Quantifying Part-to-Part Flow Variations and Cooling Effectiveness in Engine-Run Blades

Kelsey E. McCormack[1]
The Pennsylvania State University,
State College, PA 16801
e-mail: kzm233@psu.edu

Nicholas L. Gailey
The Pennsylvania State University,
State College, PA 16801
e-mail: nlg5161@psu.edu

Reid A. Berdanier
The Pennsylvania State University,
State College, PA 16801
e-mail: rberdanier@psu.edu

Michael D. Barringer
The Pennsylvania State University,
State College, PA 16801
e-mails: mdb22@psu.edu; mbarringer@psu.edu

Karen A. Thole
The Pennsylvania State University,
State College, PA 16801
e-mail: kthole@psu.edu

As turbine inlet temperatures continue to increase for modern gas turbine engines, the lifing of hot section components operating in a range of environments is becoming increasingly challenging. Engine operations in harsh environments can cause a reduction in cooling capability leading to reduced blade life relative to existing experience. This study analyzes the effects of harsh environments on the deterioration of blade flow and cooling effectiveness in turbine blades by comparing three commercially operated engines with varied operational times referenced against a baseline blade. Spatially resolved surface temperatures measured using infrared thermography at high-speed rotating conditions were evaluated to determine variations in cooling effectiveness as a function of engine operation and blade-to-blade variability from the different commercial applications. Engine-run blades were found to have reduced flow as well as greater part-to-part variation when compared to baseline blades. Blade surface temperature measurements on the deteriorated operational blades indicated film cooling traces dissipated closer to the hole exit relative to baseline blades. Furthermore, the cooling effectiveness varied significantly even between blades from the same engines. The reduction in cooling effectiveness in the engine-run blades led to higher blade temperatures and significantly shorter component life, with some exhibiting as much as an 18% reduction in life compared to baseline blades. This knowledge allows lifing models to be developed toward predicting blade operational effects in harsh environments. [DOI: 10.1115/1.4063518]

Keywords: fluid dynamics and heat transfer phenomena in compressor and turbine components of gas turbine engines, heat transfer and film cooling, measurement techniques, turbine blade and measurement advancements

Introduction

Gas turbine designers continue to increase turbine inlet temperatures to improve efficiency, resulting in flow temperatures well over 400 °C hotter than the melting temperatures of metal components in the main gas path [1,2]. Although airfoil cooling designs, along with thermal barrier coatings (TBCs), are able to protect hot gas path components throughout their intended life, vane and blade surfaces degrade differently because of environmental impacts. Over cycle times, airfoils experience spallation, erosion, hot corrosion, and particle deposition [3]. These deterioration mechanisms are particularly dramatic when operating in harsh environments with a significant density of particulates that are ingested into the engine.

Advanced cooling designs can protect components exposed to the hot gas path and extend part life. However, even in newly manufactured blades, part-to-part variations cause differences in cooling performance with respect to the design intent [4,5]. Compounded with environmental effects, manufacturing variability of components can lead to significant variability in engine operational times.

In this paper, spatially resolved blade temperatures are measured and analyzed while operating at engine scale conditions to understand the effects of operating environments relative to a set of baseline blades. The blades examined in this study were operated in aircraft engines around the world, experiencing varying levels of deterioration and, as a result, changes in overall cooling effectiveness. These blades were placed in a test turbine whereby spatially resolved temperatures were measured using infrared (IR) thermography.

Literature Review

As blades operate over time, TBC deteriorates, and film cooling performance decreases. These coatings experience a variety of deterioration mechanisms [6], many of which lead to increased surface roughness [7,8] and external heat transfer [3,9–11]. Erosion and spallation commonly occur near cooling holes, which therefore, affect the trajectory of the film in these regions [8–10]. In addition, particles have been shown to deposit on part surfaces or in cooling

---

holes, causing blockages that increase heat transfer to the blade [11,12]. This deposition occurs most often at high temperatures and increased impingement angles, as well as for large particle sizes and high velocities [13,14].

Deterioration effects are compounded by manufacturing variability of turbine parts, which can also cause deviations in film cooling performance. Factors of the manufacturing process can lead to variations in blade geometries [4] and impact blade film cooling [5,15]. Depending upon the application method, often the TBC can partially block film cooling holes [7], leading to decreased cooling performance in newly manufactured parts [16,17]. This variability only worsens during engine operation.

Deterioration is accelerated for parts operating in harsh environments, thereby shortening blade life. For example, calcia–magnesia–alumina–silicate (CMAS) particles, sand, dirt, and other small particulates found commonly in certain parts of the world often cause significant damage to turbine hardware [18,19]. As a specific example, engines operated in the Vietnam War were removed from service after an average of 80 h due to extreme compressor blade erosion [20]. Similarly, blades from Army rotorcrafts operated in Southwest Asia more recently showed significant damage due to CMAS attack and extreme deterioration [21]. The severity of this deterioration means that the operating environment typically has an important effect on blade life, which differs from the expected blade lifing per the design.

As further evidence of deterioration effects, Sidwell and Darmofal [22] found that an airline operating shorter flights with higher ambient temperatures had much shorter mean engine life compared to airlines operating at lower ambient temperatures. Investigations have predicted blade life to be reduced by 50% for temperature increases between 25 °C and 40 °C [23–26]. These estimates were used by Knisely et al. [5], who showed how manufacturing differences affected flow and cooling effectiveness. Similar to the study reported in this paper, Knisely et al. used an IR thermal imaging technique to measure blade surface temperatures and reported on the variability that can occur. These temperatures were then scaled to real-engine values using data from the NASA E^3 engine [27], showing life reductions of up to 50% due to manufacturing variations alone. Similar methods to this study will be used in the present paper, but will be applied to engine-run deteriorated blades instead of newly manufactured blades.

While many papers have been discussed that analyzed turbine blade deterioration, only a few of these studies have used actual turbine hardware. Even fewer employ data collected from blades operating at engine-relevant conditions. In addition to the previously mentioned study by Knisely et al. [5], there have been other recent studies using IR thermography to spatially resolve blade surface temperatures in a rotating environment. Lemieux [28] and Markham et al. [29] both used IR cameras to measure temperatures inside of in-service gas turbines, while additional studies have used infrared cameras in rotating turbine rigs to view blade tips and endwalls [30–32].

Michaud et al. [33] used IR imaging to analyze the overall cooling effectiveness of engine-run nozzle guide vanes (NGVs) in an annular cascade. Both mid-life and end-of-life parts run in non-sandy environments were compared to new parts with the same geometries. They found that area-averaged overall cooling effectiveness decreased for engine-run parts, particularly on the pressure side and early suction side near the leading edge. End-of-life vanes were expected to have much higher surface temperature increases at engine conditions, by up to 65 °C on the pressure side. Their study also found that superposing the effects of individual deterioration features was not able to accurately predict variations in cooling effectiveness, and that testing at engine-representative conditions is necessary to understand true performance. While this study provides important information on how parts can deteriorate over their lifetime, it does not compare variations in different operating environments, which the present paper will address.

The purpose of this study is to examine the effects of deterioration in harsh environments on overall cooling effectiveness and blade life. Our study is unique because the data presented compares both flow variations and overall effectiveness levels in engine-operated parts from both harsh and benign environments around the world. These variations were quantified for both different engine operational environments and different blades within the same engine. The use of IR thermography allowed for spatially resolved temperature and cooling effectiveness measurements across the entire blade pressure and suction surfaces while operating at engine-relevant conditions. The focus of this paper is the data on the pressure side near the blade tip, as this location is often found to exhibit relatively hotter surface temperatures. These temperatures were then scaled to real-engine temperatures to calculate expected blade life.

Facility and Instrumentation

Testing for this study was carried out at the Steady Thermal Aero Research Turbine (START) Laboratory. START houses an open loop, continuous duration turbine test facility that operates at engine-relevant conditions matching Mach, Reynolds, Rotational Reynolds, and Biot numbers. Matching these nondimensional parameters to that of an engine provides the ability to scale measured temperatures at test conditions to that of engine conditions. An overview of the facility can be seen in Fig. 1. More information about this facility is described by Barringer et al. [34], with updates detailed by Berdanier et al. [35].

The START facility uses two centrifugal compressors to supply up to 10.4 kg/s (25 lbm/s) of air to the turbine. Air exits the compressors at a pressure of up to 480 kPa (70 psia) and a temperature of 395 K (250 °F). Most of this air goes into the main gas path, but a portion is split off to use as cooling air. The cooling air is sent through a shell-and-tube heat exchanger to lower the temperature to 273 K (32 °F), after which it can be used for three controlled cooling supplies: vane trailing edge (VTE) flow, tangential on-board injection (TOBI) flow through the rotating blades, and purge flow to seal the under-platform cavity.

Air in the main gas path is sent through a natural gas burner, where the temperature can be heated as high as 672 K (750 °F). However, a lower temperature was used for this study due to instrumentation requirements. Main gas path temperatures are measured by six thermocouples upstream of the vane at varied circumferential locations. Temperatures of each cooling flow are measured prior to their introduction to the test section. The START rig contains a single-stage turbine test section, with one row each of vanes and blades. All blades were previously operated engine hardware, which will be further described in the following sections.
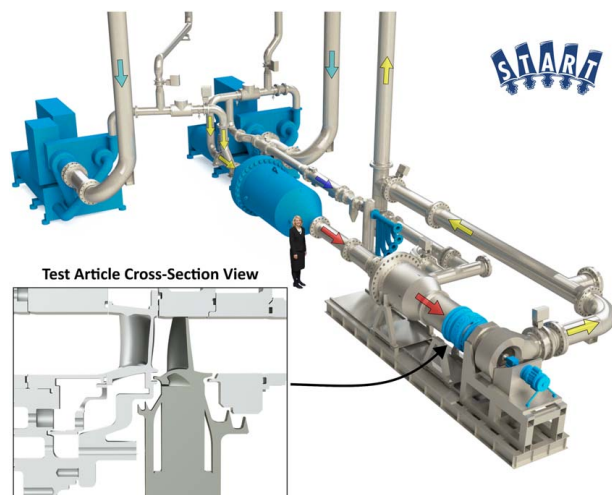

Fig. 1 START facility with single-stage turbine test section

Infrared Thermography Measurements. The START facility utilizes IR imaging to capture temperatures on turbine blade surfaces as they rotate at over 10,000 RPM. START's IR system, which was first described by Knisely et al. [36], used a mercury-cadmium-telluride detector in the long-wavelength spectrum. The detector was mounted on top of the START rig, where an optical probe was inserted through the rig casing at different axial positions to capture the images of the blade surface during operation. To view the pressure side and leading edge of a blade, the optical probe was placed in a specially designed, additively manufactured vane upstream of the blades with a viewing window cut from the vane's suction side, as seen in Fig. 2. In addition, a separate measurement port was made to capture the suction side, which is not the focus of this paper. The position of the probe in the vane was such that its placement did not affect the blade being imaged, as verified through computational fluid dynamics (CFD).

The camera angle and radial position were modified throughout testing to take images that encompassed the entire pressure side, suction side, and leading-edge surfaces. Two hundred images were captured at each viewing location and averaged to reduce noise in the final image. A camera integration time of 2 μs was shown by Knisely et al. [36] to reduce both motion blur and noise during operation and was therefore used for all images in this study. Phase locking allowed for consistent identification and imaging of specific individual blades as they rotated during testing.

Calibration images were performed to correlate the raw pixel values measured by the camera with detected radiation based on surface temperature. To perform these calibrations, images were taken of a copper plate coated in high-emissivity black paint. The temperature of this plate was varied over the entire range of blade surface temperatures expected during testing. The raw pixel values of the camera were then correlated with the expected radiation based on emissivity, surface temperature, and background temperature during the individual calibration. By using this calibration procedure, blade surface temperatures were calculated using only emissivity and rig background temperature during data acquisition. Once completed, the measured temperatures were mapped onto the blade surface through in-house software that was developed by the investigators.

While images were taken of the entire pressure and suction surfaces, this paper primarily focuses on the pressure side tip trailing edge region, shown in Fig. 3. Area-averaged overall effectiveness was calculated in Region A, where Region A contains a row of four radially spaced cooling holes. Additional analysis focused on film cooling trajectories, all of which were calculated for the hole shown in Region B.

Overall cooling effectiveness was used to compare the cooling performance. Cooling effectiveness is a nondimensional temperature that provides the needed scaling between test turbine and engine blade temperatures, provided the relevant nondimensional parameters are matched to that of the engine. Effectiveness was
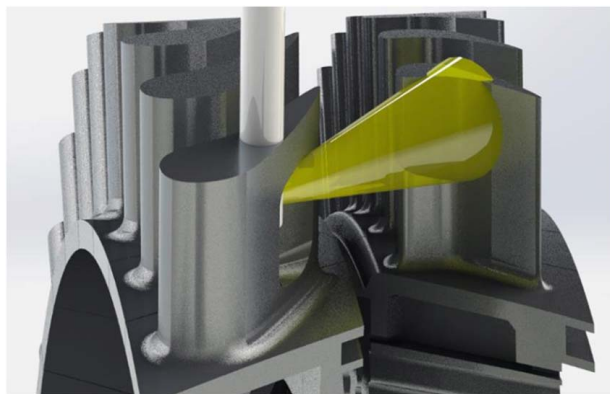

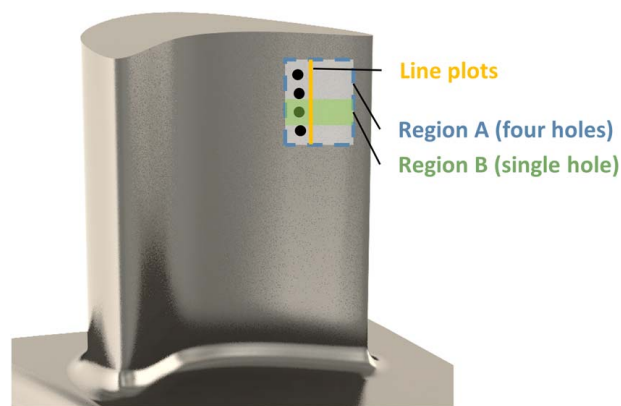**Fig. 2 IR probe location in the START rig**

Fig. 3   Analysis locations of tip trailing edge and mid chord regions

calculated using Eq. (1), using main gas path temperature, blade surface temperature, and cooling air temperature. Blade temperatures were measured using IR thermography, while main gas path and cooling temperatures were measured with thermocouples as described in the facility instrumentation section. Because Reynolds number, Mach number, and Biot number were matched to engine conditions, calculated effectiveness could be used to scale values to true engine temperatures.

$$\phi = \frac{T_{\mathrm{mgp}} - T_s}{T_{\mathrm{mgp}} - T_c} \tag{1}$$

All the data presented in this paper are comparisons of the degradation of the cooling performance using effectiveness values due to environmental impacts relative to a baseline condition.

Uncertainty and Repeatability. Uncertainty in temperature and effectiveness was calculated using methods described by Moffat [37]. The main contributors to bias uncertainty were the calibration, surface emissivity, and background temperatures. For precision uncertainty, the main contributor is the IR detector's pixel value.

Looking at the bias uncertainty contributions, the calibration uncertainty is dependent on the thermocouples measuring surface and background temperature during the calibration, the emissivity measurement of the calibration surface, and the error introduced by the curve fit correlating the raw pixel values of the camera with measured radiation. The uncertainty of emissivity values for this set of blades was measured, and all contributing temperatures were used to calculate background temperature uncertainty. The precision uncertainty within a 95% confidence interval was calculated for each pixel across the 200 images taken for a given position. For the data reported in this paper, the bias uncertainty of the relative effectiveness values when compared to a baseline condition $(\phi - \phi_{\mathrm{bl}}/\phi_{\mathrm{bl}})$ was calculated to be 0.046, while the precision uncertainty based on the 200 images was 0.037.

To map the images into one composite of the blade surface, consistent and repeatable test conditions in START were required to be replicated over many test days. As an illustration of the repeatability, Figs. 4(a) and 4(b) show the blade surface temperature and overall effectiveness behind the row of cooling holes in Region A. The solid and dotted lines for a given color show data taken at the same test condition on different days. The measurements almost entirely overlap, with only slight variations directly behind cooling holes. The typical repeatability from day to day was $\phi/\phi_{\mathrm{max}} = 0.003$, while the maximum repeatability differences were 0.015.

Description of Blades Tested. Four sets of blades were tested in this study: one baseline and three operated in engines under different conditions and cycles. All blades had the same geometry and
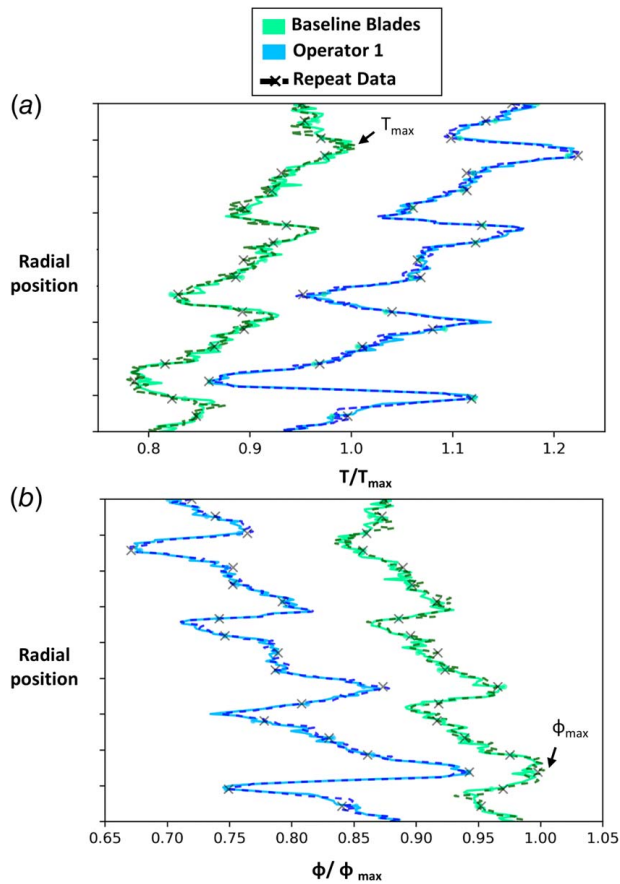
Fig. 4 (a) Surface temperature and (b) cooling effectiveness for baseline and operator 1 blades plotted behind a row of cooling holes as shown in Fig. 3. Dotted lines represent the same data taken on a separate test day.

cooling design. Run times were compared to the run time of a set of baseline blades through a nondimensional Δt shown in Eq. (2). The run time of the baseline blades was subtracted from each operator, and the entire value was divided by the maximum run time minus the baseline run time.

$$\Delta t = \frac{t - t_{\text{baseline}}}{t_{\text{max}} - t_{\text{baseline}}} \qquad (2)$$

The environmental and operational impacts for blades of different operators can be seen in Fig. 5. These sample images were chosen from the pressure side. Baseline blades, shown in Fig. 5(a), have a uniform TBC surface, showing no signs of deterioration as would be expected. Figure 5(b) shows the surface sample for operator 1 for a benign environment, with a $\Delta t = 1$, having a slight discoloration and deterioration on the surface. The
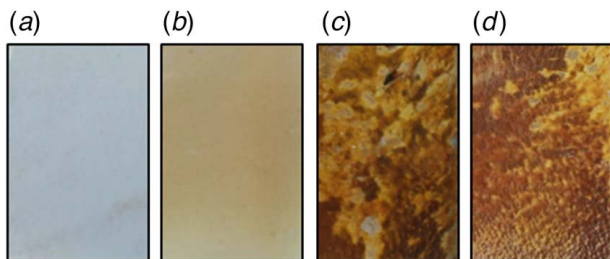
TBC for operator 1, however, is still mostly intact. This level of deterioration is expected for the benign environment that operator 1 blades experienced. Operators 2 and 3 were in a harsh environment, with Δt of 0.75 and 0.4, respectively, and show significant deterioration levels, including TBC spallation revealing bare metal surfaces. As evidenced in these photos, operators 2 and 3 were operated in much harsher environments with high CMAS attack, leading to higher levels of deterioration with shorter run times. All operators showed the highest deterioration levels on the pressure side and leading edge.

Blade Flow Variations

Each of the test blades was characterized in terms of their post-operational flow parameter (FP) versus pressure ratio (PR) characteristics. FP encompasses the mass flow weighted by a particular pressure and temperature. Because the turbine test rig sets mass flow for an entire row of blades, the FP is needed to determine the mass flow split for each specific blade. Separate FP measurements were made for the individual internal cooling passages for each blade. To determine the FP, benchtop flow testing was conducted for each component at a set PR and temperature while measuring the mass flow.

The median FP for a particular pressure ratio for each operator is shown in Fig. 6. The range bars show the minimum and maximum flow within an operator. Each value is normalized by the maximum FP of the baseline blades, which had the highest of the four blade sets tested.

Figure 6 shows that operator 3 blades with the lowest run time had the highest flow parameter at 82% of the baseline blade maximum, even though these blades were operated in a harsh environment. The median flow blade of operator 1 had a very similar flow parameter to that of operator 3 even though it had the highest run time, illustrating the engine-to-engine variability. Operational and environmental impacts combine to determine the degradation of parts, which is illustrated by the similarities between flow parameters for operator 1 in a benign environment with a much higher run time than operator 3 in a harsh environment. Operator 2 blades were the most deteriorated and had the lowest FP, with the minimum flowing blade as low as 70% of the maximum baseline blade flow. The results for operator 2, also operated in a harsh environment, were because of cooling hole blockages and internal channel deposits.

Operator 2 blades were run in a similar harsh environment as operator 3 but for a longer run time and have nearly twice as much variation in flow parameter. Even though operator 1 blades have the longest run time, they have more similar ranges in flow parameter to operator 3 blades. Harsh environments appear to have caused less consistent deterioration in blades, leading to large variations in flow even within blades from the same engine.
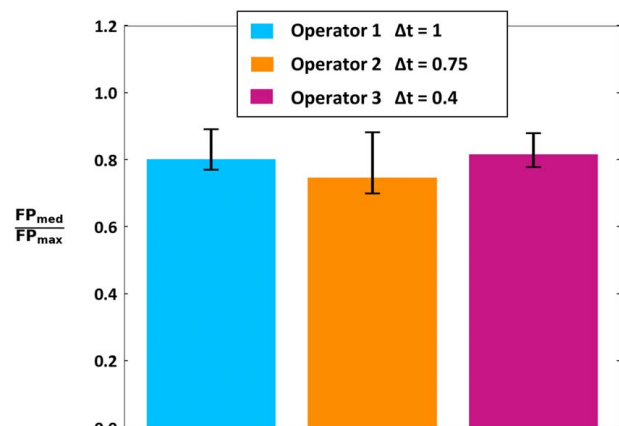

Fig. 5 Images of blade deterioration for (a) baseline blades ($\Delta t = 0$), (b) operator 1 (benign, $\Delta t = 1$), (c) operator 2 (harsh, $\Delta t = 0.75$), and (d) operator 3 (harsh, $\Delta t = 0.4$)

Fig. 6 Median flow parameter for each operator

Blade Durability Impacts From the Environment

As previously described, thermal images of both the pressure and suction sides of the operational blades placed in the rainbow turbine stage were measured. These images were appropriately calibrated and then mapped onto the surface of the blades. It is important to note that temperatures were measured at the surface, which in some cases was intact TBC but where TBC deteriorated represented the metal temperature. Thermal images were appropriately calibrated to account for this variation. Surface temperatures were then put in the form of overall effectiveness, which is a nondimensional temperature that uses the upstream main gas path temperature as well as the coolant temperature measured in the cavity supplying the blade root.

The data presented in this section is an augmentation of the overall cooling effectiveness relative to the set of baseline blades at 80% span for the pressure side. The particular blades that were chosen were those with the median cooling flow.

For all cases, the data shown in Fig. 7 show significant deterioration of the overall effectiveness levels, meaning higher blade temperatures would be expected when operating in the engine. The horizontal line in Fig. 7 represents "0," meaning there is no augmentation relative to the baseline set of blades at that span location. The 0% length occurs at the leading edge of the blade. As the data in Fig. 7 approach zero, it means that there is less degradation since it is closer to the baseline set of blades. Note that exact values are not provided, but, rather, this data is used to compare the relative impacts of the environment. The spikes shown in Fig. 7 occur where there are either cooling holes or image mapping fiducial marks.

In reviewing the data presented in Fig. 7, the reduction of the overall effectiveness is the most similar and the worst for operators 2 and 3, with higher degradation in part because of the operation in harsh environments unlike operator 1. These large decreases in effectiveness occurred on the pressure side at 80% span for all operators where TBC had deteriorated on the engine-run blades.

It is interesting to note that the deterioration relative to the baseline blades indicated the biggest differences between −70% > Length (%) > −100%, where all three environmentally impacted airfoils showed higher values of effectiveness augmentation. The increased augmentation levels indicate that the tip trailing edge was less impacted by environmental factors when compared to the rest of the pressure side surface.

Area-Averaged Cooling Effectiveness. Specific area-averaged cooling effectiveness measurements were made in the region where the blades experienced the highest temperatures. The trailing edge tip region on the pressure side was shown to have the hottest temperatures, which is illustrated in Fig. 3 in Region A. Blades presented in the following figures were the median flow blade within
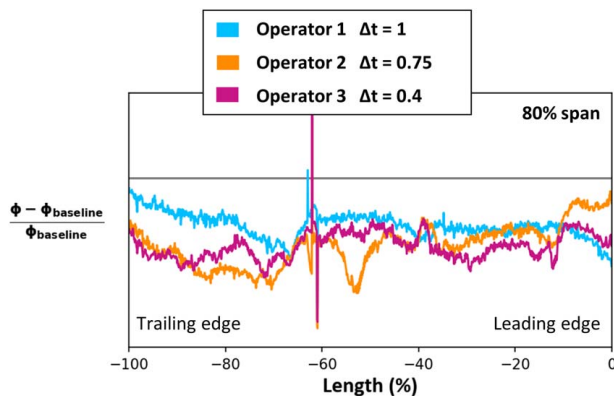
Fig. 7 Cooling effectiveness around the blade at 80% span. Horizontal line is the "0" value meaning no augmentation relative to the baseline blades
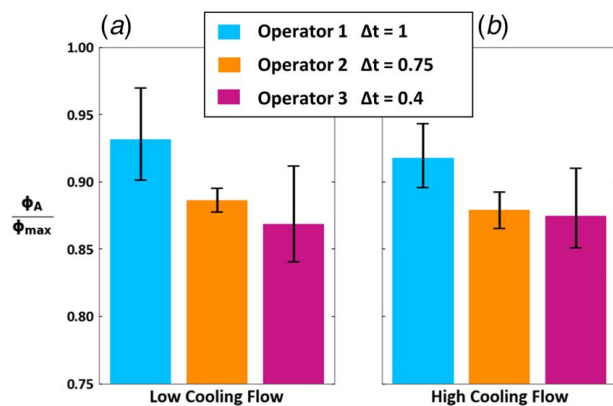
Fig. 8 Area-averaged cooling effectiveness in tip trailing edge region for (a) low and (b) high cooling flow conditions

each operator, with error bars showing values for the minimum and maximum flow blade.

Figure 8 shows the area-averaged cooling effectiveness for a low and high cooling flow condition for the three operators relative to the baseline set of blades. Note that all values are normalized by the maximum overall effectiveness of baseline blades. The data in Fig. 8 indicate that all operators showed a reduction in effectiveness from the baseline blades, with the largest reductions in effectiveness seen for the harsh operators 2 and 3.

Even though the blades were operated in a benign environment, in this particular region of the blade for operator 1 with the highest run times, the effectiveness augmentation is still as much as 7% lower than the baseline blade maximum.

For lower coolant flows, operator 3 was lower by 2% relative to operator 2 as shown in Fig. 8. At a high cooling flow, the effectiveness augmentation varied by less than 1% between operators 2 and 3. This was true even though operator 3 blades had a much lower run time than operator 2 and were expected to have experienced less deterioration.

Figure 8 shows that the variability between the blades for operator 3 was higher than the other operators 1 and 2 at both cooling flow conditions. This data indicates that higher variability between blades can occur at shorter operational times in harsh environments.

Film Cooling Trajectories. Applying the methods reported by Knisely et al. [5], specific film cooling trajectories were evaluated using IR images. For the method previously reported by Knisely, the coordinate of the cooling hole start (s') was mathematically defined by using the highest slope in effectiveness along the coolant trajectory. This method was needed since the cooling hole breakouts cannot be detected given the conduction effects. A depiction of the method previously used by Knisely et al. applied to baseline blades is shown in Fig. 9 [5]. The downstream trajectory of the coolant was then defined using the measured temperatures having the maximum effectiveness.

While this method had previously been used successfully with newly manufactured blades, it was much more challenging for deteriorated blades due to hole blockage and other effects. Trajectories were less clear for deteriorated blades, with the coolant dissipating close to the hole exit or even blowing off the surface. Cooling holes may have been blocked or had very different trajectories due to dirt deposition and TBC deterioration.

Because coolant trajectories could not be determined due to either no coolant trace or blow off from the surface for the deteriorated blades, the coolant trajectory from the baseline blade was used to define the coordinate system for the cooling holes of engine-run blades. Stated another way, the trajectory of the coolant from the baseline blades was applied to the deteriorated blades. The case for the baseline blade chosen to define the trajectory was that of
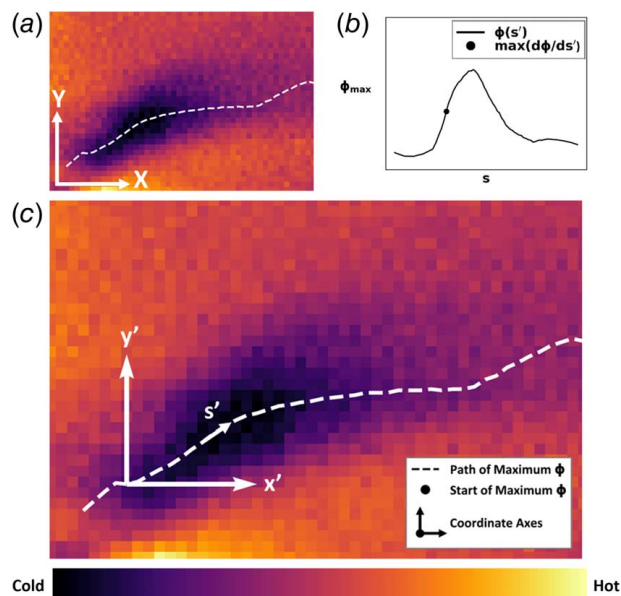
Fig. 9 Film cooling trajectory method applied to baseline blades, including (a) cooling hole with the path of maximum effectiveness applied, (b) illustration of the maximum slope to define s′ = 0 at the start of the trace, and (c) cooling trace applied to a cooling hole

the mean flow blade to provide a comparison of overall effectiveness between operators.

Figures 10(a)–10(c) show an illustration of how the coolant trajectory method just described was applied to the deteriorated, engine-operated blades. Figure 10(a) illustrates the contours from a single harsh operator cooling hole, whereas Fig. 10(b) illustrates the trajectory defined on the baseline blade for the maximum cooling effectiveness, as described by Knisely et al. [5]. Finally, Fig. 10(c) illustrates the coolant trajectory locations based upon the baseline blades in Fig. 10(b) applied to the engine-operated blade. While the trajectory does not fully represent what is happening in the engine-operated blade, it does allow for a consistent
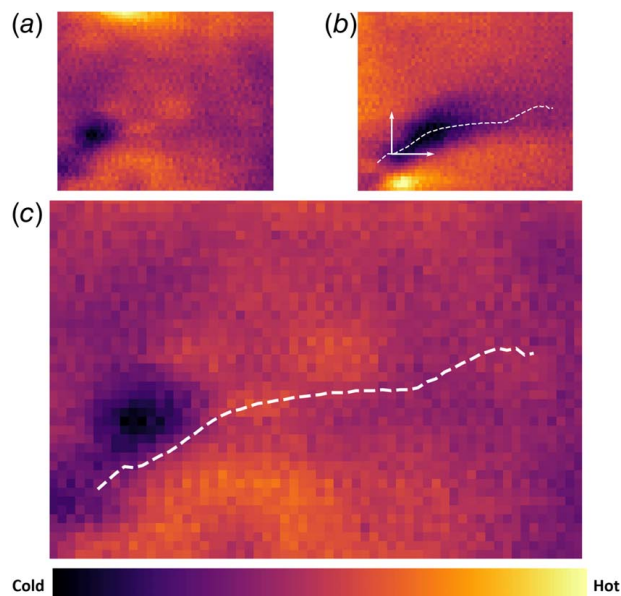

Fig. 10 (a) Cooling hole on an engine-operated blade, (b) cooling hole region with applied trajectory for a baseline blade, and (c) cooling hole on an engine-operated blade with trajectory from a baseline blade applied

method in defining a cooling trace and does provide a comparison of cooling variations due to environmental impacts.

Baseline blades, with the shortest run time, were shown to have clearly present trajectories, as seen in Fig. 10(b). There is a region of increased cooling effectiveness starting at the cooling hole, which carries behind the hole as the coolant air reduces blade surface temperature. However, the operator 3 blades run in a harsh environment, as shown in Fig. 10(c), have a decreased temperature at the cooling hole only. While there is a cold region where coolant air exits the hole, the flow does not stay attached to the surface and therefore there is no region of increased effectiveness behind the hole. Deterioration or blockage of film cooling holes alters the flow and cooling, which was measured most predominantly for operators 2 and 3, both having high CMAS levels due to harsh environments. This lack of cooling leads to higher surface temperatures, which shorten the blade operational life.

The effectiveness value along the film trajectory for the minimum, median, and maximum flow blade of each operator is plotted in Fig. 11 for Region B in Fig. 3. The case chosen to evaluate was for a high coolant flow. The shaded region in Fig. 11 notes the range of the blade flows over all four operators, and the dashed lines show the median flow blade of each operator. Data for all blades within each operator can be seen in Fig. 12. All values are normalized by the maximum overall effectiveness of a single baseline blade.

Figure 11 shows that the baseline blades have a high effectiveness for six-hole diameters downstream of the cooling hole shown in Fig. 11. However, the effectiveness values decrease closer to the hole for engine-operated blades. While the median flow blade of operator 1 had a slightly higher effectiveness than operators 2 and 3, there was still a significant reduction from the baseline blades. The harsh environment blades of operators 2 and 3 had similarly low effectiveness, even though operator 2 blades had a longer engine run time.

To see further details relative to Fig. 11 for each blade set, the maximum effectiveness along the cooling trajectory for all blades within each operator is shown in Figs. 12(a)–12(d). The FP values were defined for the entire blade and are not specific to Region B in Fig. 3. Note that the effectiveness for each blade set was normalized by the maximum of the baseline blades. The minimum, median, and maximum flow blades are shown in dashed, dashed-dotted, and solid lines, respectively.

The baseline data in Fig. 12(a) shows less variation in the maximum cooling effectiveness for the set of baseline blades compared to those for operators 1–3. Each of the data sets for the operators had its own characteristic decay shape. The blade temperatures for operator 1 indicated nearly a flat profile for all the cases, as shown in Fig. 12(b). Since all the holes for the different flow cases resulted in the same blade temperature profile, it implies that the film cooling in this region is not dominating or that for every case the trajectory for the baseline blades does not capture the decay.
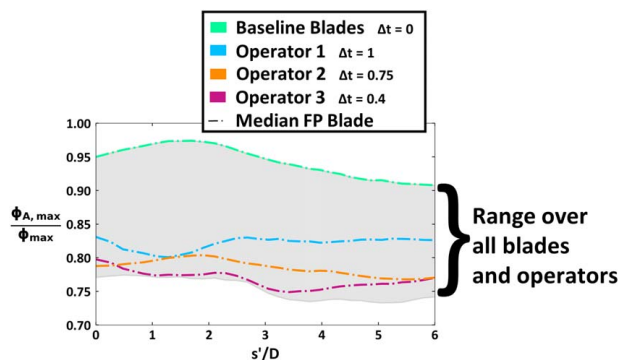

Fig. 11 Effectiveness along cooling trajectory as a function of s′/D behind a cooling hole
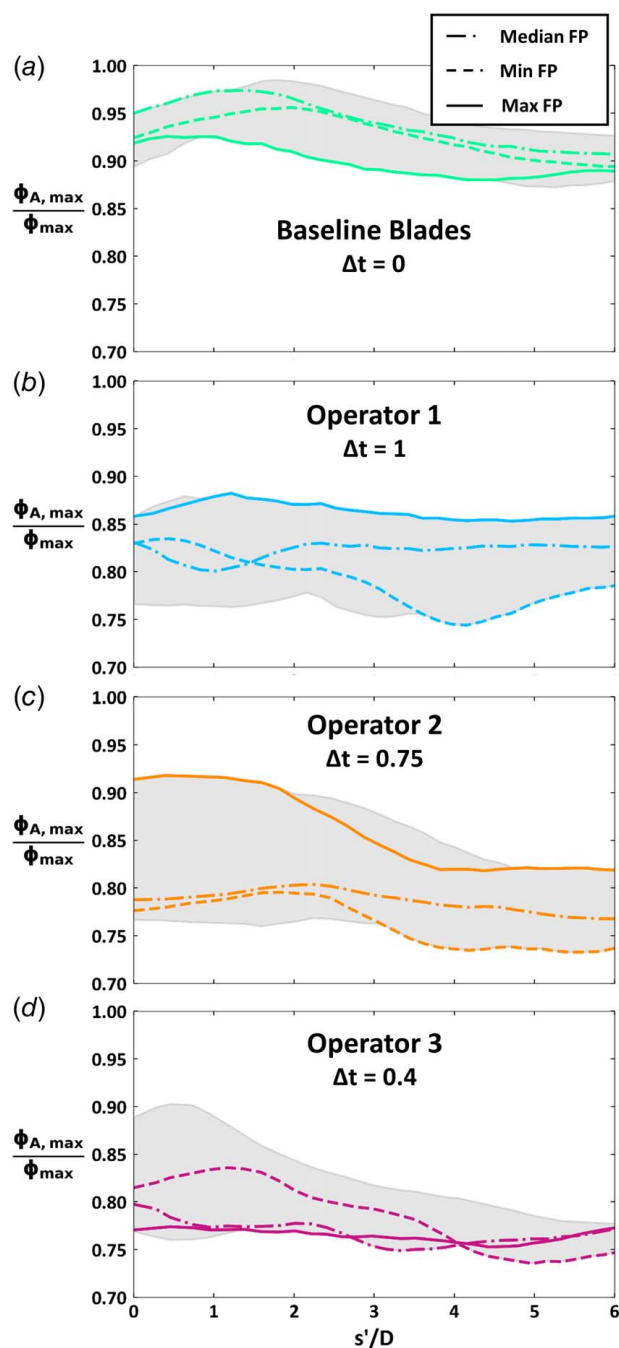
Fig. 12 Film trace overall effectiveness for (a) baseline, (b) operator 1, (c) operator 2, and (d) operator 3 blades normalized with a singular baseline blade

Table 1 NASA E³ engine temperatures

Quantity	NASA E³ value
Cooling air temperature, T_c	628 °C (1162 °F)
Main gas path air, T_∞	1396 °C (2545 °F)

blade with the maximum flow parameter had nearly the lowest cooling effectiveness behind the cooling hole. Additionally, the lowest flowing blade for three of the four blade sets had higher cooling effectiveness than the median flow blade at some point downstream of the cooling hole.

Because the flow parameter measurements were for the entire blade, they do not necessarily correlate with the amount of flow through this individual cooling hole. As blades deteriorated during operation, cooling holes were more likely to become blocked and variations in flow between individual cooling holes are expected. Even in newly manufactured blades, Knisely et al. [5] showed that flow through smaller regions did not necessarily correlate with flow through the entire blade. Total flow parameter was therefore not necessarily indicative of flow through a cooling hole, and even blades with the same amount of flow could experience different paths of cooling flow on the blade surface, thus changing the region's effectiveness.

Estimates of Blade Lifing. Scaling the data from the measured blade surface temperatures using overall cooling effectiveness, ϕ, provides the ability to use the data to estimate blade surface temperatures in an operating engine. It is noted that the operating conditions of START are at much lower pressures and temperatures relative to the engine, but given the relevant nondimensional numbers are matched to that of the engine (Re, Ma, and Bi), scaling is possible. To illustrate the impacts of the environment on the blade temperatures, a non-proprietary set of conditions was chosen to be those from the NASA E³ [27] engine. These values are shown in Table 1. For this analysis, the minimum effectiveness values (highest surface temperatures) determined from the infrared image measured on the pressure side of each blade were used for the scaling to the NASA E³ engine conditions.

Increases in scaled temperatures at E³ engine conditions can be seen plotted against the relative blade life in Fig. 13 along with an example lifing curve [5]. The bars in Fig. 13 represent the ranges in the minimum effectiveness that occurred within a particular blade set on the pressure side. The median point for operator 1 blades fell along the lifing curve, showing that current predictions can estimate blade life for benign environments as shown in Fig. 5. However, blades operated in harsh environments fell below the lifing curve, particularly operator 3 blades. Operator 3 blades had a much larger surface temperature increase than expected for the run time of these blades. These were much
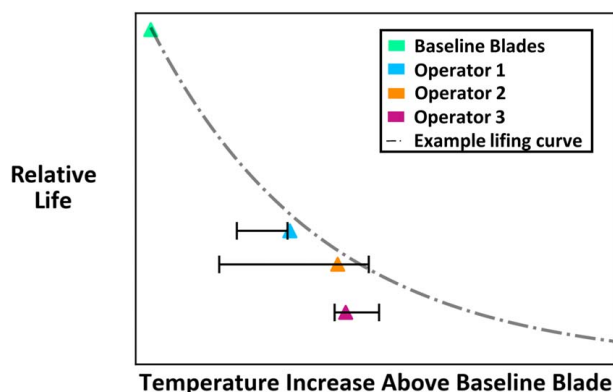
Operators 2 and 3 both have a large range of overall effectiveness at the cooling hole, as shown in Figs. 12(c)–12(d). The data also shows that the coolant significantly decays after only one- or two-hole diameters. Further from the cooling hole, the flow appears to be detached and effectiveness is low for all blades operated in harsh environments. However, the maximum effectiveness directly at or behind the hole is higher for some of the harsh operator blades than for the benign operator blades, even though it does decrease significantly further from the hole.

Although blades with higher flow parameters would be expected to have higher cooling effectiveness, this was not the case for many of the blades shown in Figs. 12(a)–12(d). The maximum flow blade did have the highest cooling effectiveness for operators 1 and 2 but not for the baseline blades or operator 3. For the baseline blades, the

Fig. 13 Blade life curve with baseline and operator 1–3 blades

worse than the operator 2 blades, which had a similar increase in surface temperature but a much longer run time. This decrease in life resulted from the high levels of deterioration that occurred in the heavy CMAS environment, causing decreased cooling performance and shortened life for these blades.

Conclusions

This study determined the effects of engine operation across varied environments on flow and cooling effectiveness. Three operators, all with different run times and environments, were compared with a set of baseline blades. The environments included operator 1 from a benign environment and operators 2 and 3 from harsh environments. The changes in flow and cooling effectiveness due to deterioration in both benign and harsh environments were then compared through multiple approaches.

Flow parameters were measured at a given pressure ratio for all blades in this study. The median flow parameter was highest for baseline blades, with reductions in FP of almost 30% for blades operated in harsh environments. In addition to variations between operators, large flow parameter variations within the same operators indicated that blades did not deteriorate uniformly even when operated at the same conditions.

Overall effectiveness levels were analyzed along the pressure side near the blade tip. Harsh operators showed decreases in effectiveness being impacted at the 80% span, which coincided with regions where the TBC was absent. When looking at the tip trailing edge region, area-averaged effectiveness was very similar for both harsh operators at both high and low TOBI flowrates while being much lower than either benign or baseline blades.

Film cooling trajectories behind a specific cooling hole across all operators were compared between the blades. For the baseline blade, clear trajectories of the film were identified with the location applied to all blades in this study. This showed consistently high cooling effectiveness downstream of cooling holes for baseline blades, while effectiveness dissipated close to the hole for deteriorated blades. Effectiveness showed large variations immediately downstream of cooling holes in engine run operators, but low effectiveness values after one- or two-hole diameters for all deteriorated blades.

Effectiveness values in this study were used to predict blade surface temperatures scaled to the NASA E^3 engine. This showed large increases in surface temperature at true engine conditions, leading to a significant reduction in expected life when compared to published lifing models.

This study provides a new understanding of how blade flow and overall blade temperatures vary based on part deterioration levels and the impacts of different environmental effects. The results presented give a good indication of the part-to-part variations in deterioration between operators and even within the same operator. This knowledge will help to improve blade lifing models for a range of run times and operational environments.

Conflict of Interest

There are no conflicts of interest.

Data Availability Statement

The datasets generated and supporting the findings of this article are obtainable from the corresponding author upon reasonable request.

Nomenclature

D = film cooling hole diameter
P = absolute pressure
T = temperature
X = global horizontal coordinate in image (pixels)
Y = global vertical coordinate in image (pixels)
$\dot{m}$ = mass flowrate
s' = path distance along cooling jet trajectory
x' = axial distance downstream of cooling hole
y' = radial distance downstream of cooling hole
FP = flow parameter $(\dot{m}\sqrt{T_{in}}/P_{out})$
PR = pressure ratio (P_{in}/P_{out})
Δt = $(t - t_{baseline})/(t_{max} - t_{baseline})$

Greek Symbols

Δ = difference
φ = overall effectiveness $(T_\infty - T_s)/(T_\infty - T_c)$

Subscripts

c = cooling air
s = blade surface
A = area-averaged
in = channel inlet
max = maximum flow parameter
med = median flow parameter
min = minimum flow parameter
out = outlet
∞ = mainstream

References

[1] Bunker, R. S., 2017, "Evolution of Turbine Cooling," Proceedings of ASME Turbo Expo, Paper No. GT2017-63205.
[2] Saravanamuttoo, H., Rogers, G., Cohen, H., and Straznicky, P., 2009, *Gas Turbine Theory*, Pearson Education Limited, Harlow, UK.
[3] Meher-Homji, C. B., and Gabriles, G., 1998, "Gas Turbine Blade Failures—Causes, Avoidance, and Troubleshooting," Proceedings of the 27th Turbomachinery Symposium, Houston, TX, pp. 129–180.
[4] Bunker, R. S., 2009, "The Effects of Manufacturing Tolerances on Gas Turbine Cooling," ASME J. Turbomach., **141**(4), p. 041018.
[5] Knisely, B. F., Berdanier, R. A., Wagner, J. H., Thole, K. A., Arisi, A. N., and Haldeman, C. W., 2023, "Effects of Part-to-Part Flow Variations on Overall Effectiveness and Life of Rotating Turbine Blades," ASME J. Turbomach., **145**(6), p. 061016.
[6] Hamed, A., Tabakoff, W. C., and Wenglarz, R. V., 2006, "Erosion and Deposition in Turbomachinery," J. Propul. Power, **22**(2), pp. 350–360.
[7] Bogard, D. G., Schmidt, D. L., and Tabbita, M., 1996, "Characterization and Laboratory Simulation of Turbine Airfoil Surface Roughness and Associated Heat Transfer," ASME J. Turbomach., **120**(2), pp. 337–342.
[8] Bons, J. P., Taylor, R. P., McClain, S. T., and Rivir, R. B., 2001, "The Many Faces of Turbine Surface Roughness," Proceedings of ASME Turbo Expo, Paper No. GT-2001-0163.
[9] Ekkad, S. V., and Han, J. C., 2000, "Film Cooling Measurements on Cylindrical Models With Simulated Thermal Barrier Coating Spallation," J. Thermophys. Heat Transfer, **14**(2), pp. 194–200.
[10] Ekkad, S., and Han, J.-C., 1997, "Detailed Heat Transfer Distributions on a Cylindrical Model With Simulated TBC Spallation," Proceedings of the 35th Aerospace Sciences Meeting and Exhibit, Reno, NV, Jan 6–9, pp. 97–0595.
[11] Lawson, S. A., and Thole, K. A., 2011, "Effects of Simulated Particle Deposition on Film Cooling," ASME J. Turbomach., **133**(2), p. 021009.
[12] Sundaram, N., and Thole, K. A., 2007, "Effects of Surface Deposition, Hole Blockage, and Thermal Barrier Coating Spallation on Vane Endwall Film Cooling," ASME J. Turbomach, **129**(3), pp. 599–607.

[13] Singh, S., and Tafti, D., 2015, "Particle Deposition Model for Particulate Flows at High Temperatures in Gas Turbine Components," Int. J. Heat Fluid Flow, **52**, pp. 72–83.

[14] Hamed, A. A., Tabakoff, W., Rivir, R. B., Das, K., and Arora, P., 2005, "Turbine Blade Surface Deterioration by Erosion," ASME J. Turbomach., **127**(3), pp. 445–452.

[15] DeShong, E. T., Berdanier, R. A., and Thole, K. A., 2023, "Predictive Modeling of Local Film-Cooling Flow on a Turbine Rotor Blade," ASME J. Turbomach., **145**(4), p. 041014.

[16] Bunker, R. S., 2000, "Effect of Partial Coating Blockage on Film Cooling Effectiveness," Proceedings of ASME Turbo Expo, Paper No. GT-2000-0244.

[17] Whitfield, C. A., Schroeder, R. P., Thole, K. A., and Lewis, S. D., 2015, "Blockage Effects From Simulated Thermal Barrier Coatings for Cylindrical and Shaped Cooling Holes," ASME J. Turbomach., **137**(9), p. 091004.

[18] Ramirez Velasco, J. H., Petrosky, K., Kilaz, G., Kenttämaa, H., and Trice, R. W., 2021, "Thermochemical Interaction of Biofuel Impurities With Yttria-Stabilized Zirconia Thermal Barrier Coatings," Ceram. Int., **47**(17), pp. 24675–24682.

[19] Murugan, M., Ghoshal, A., Walock, M., Nieto, A., Bravo, L., Barnett, B., Pepi, M., et al., 2017, "Microstructure Based Material-Sand Particulate Interactions and Assessment of Coatings for High Temperature Turbine Blades," Proceedings of ASME Turbo Expo, Paper No. GT2017-64051.

[20] Mund, M. G., and Guhne, H., 1970, "Gas Turbines—Dust—Air Cleaners: Experience and Trends," Proceedings of ASME Gas Turbine Conference, Paper No. 70-GT-104.

[21] Murugan, M., Ghoshal, A., Walock, M. J., Barnett, B. B., Pepi, M. S., and Kerner, K. A., 2017, "Sand Particle-Induced Deterioration of Thermal Barrier Coating on Gas Turbine Blades," Adv. Aircr. Spacecr. Sci., **4**(1), pp. 37–52.

[22] Sidwell, V., and Darmofal, D., 2003, "Probabilistic Analysis of a Turbine Cooling Air Supply System: The Effect on Airfoil Oxidation Life," Proceedings of ASME Turbo Expo, Paper No. GT-2003-38119.

[23] Bogard, D. G., and Thole, K. A., 2006, "Gas Turbine Film Cooling," J. Propul. Power, **22**(2), pp. 249–270.

[24] Han, J.-C., and Wright, L. M., 2007, "Enhanced Internal Cooling of Turbine Blades and Vanes," Gas Turbine Handbook, Department of Energy, National Energy Technology Laboratory, Morgantown, WV, pp. 321–352.

[25] Bunker, R. S., Dees, J. E., and Palafox, P., 2014, "Impingement Cooling in Gas Turbines: Design, Applications, and Limitations," Impingement Jet Cooling in Gas Turbines, WIT Press, Southampton, UK, pp. 1–32.

[26] Reyhani, M. R., Alizadeh, M., Fathi, A., and Khaledi, H., 2013, "Turbine Blade Temperature Calculation and Life Estimation—A Sensitivity Analysis," Propuls. Power Res., **2**(2), pp. 148–161.

[27] Halila, E. E., Lenahan, D. T., and Thomas, T. T., 1982, "Energy Efficient Engine High Pressure Turbine Test Hardware Detailed Design Report," NASA Report No. CR-17955.

[28] Lemieux, D. H., 2005, "On-Line Thermal Barrier Coating Monitoring for Real-Time Failure Protection and Life Maximization," US Department of Energy Technical Report.

[29] Markham, J., Cosgrove, J., Scire, J., Haldeman, C., and Agoos, I., 2014, "Aircraft Engine-Mounted Camera System for Long Wavelength Infrared Imaging of In-Service Thermal Barrier Coated Turbine Blades," Rev. Sci. Instrum., **85**(12), p. 124902.

[30] Sisti, M., Falsetti, C., Beard, P., and Chana, K., 2021, "Infrared Temperature Measurements on High Pressure Turbine Blades in the Oxford Turbine Research Facility: Calibration and Image Processing Techniques," Proceedings of the 14th European Conference on Turbomachinery Fluid Dynamics & Thermodynamics, Gdansk, Poland, Apr. 12–16.

[31] Christensen, L., Celestina, R., Sperling, S., Mathison, R., Aksoy, H., and Liu, J., 2020, "Infrared Temperature Measurements of the Blade Tip for a Turbine Operating at Corrected Engine Conditions," ASME J. Turbomach., **143**(10), p. 101005.

[32] Lazzi Gazzini, S., Schädler, R., Kalfas, A. I., and Abhari, R. S., 2017, "Infrared Thermography With Non-Uniform Heat Flux Boundary Conditions on the Rotor Endwall of an Axial Turbine," Meas. Sci. Technol., **28**(2), pp. 025901.

[33] Michaud, M., Chowdhury, N., and Povey, T., 2023, "Experimental Study of Impact of In-Service Deterioration on Thermal Performance of High-Pressure Nozzle Guide Vanes," ASME J. Turbomach., **145**(2), p. 021014.

[34] Barringer, M., Coward, A., Clark, K., Thole, K. A., Schmitz, J., Wagner, J., Alvin, M. A., Burke, P., and Dennis, R., 2014, "The Design of a Steady Aero Thermal Research Turbine (START) for Studying Secondary Flow Leakages and Airfoil Heat Transfer," Proceedings of ASME Turbo Expo, Paper No. GT-2014-25570.

[35] Berdanier, R. A., Monge-Concepción, I., Knisely, B. F., Barringer, M. D., Thole, K. A., and Grover, E. A., 2019, "Scaling Sealing Effectiveness in a Stator–Rotor Cavity for Differing Blade Spans," ASME J. Turbomach., **141**(5), p. 051007.

[36] Knisely, B. F., Berdanier, R. A., Thole, K. A., Haldeman, C. W., Markham, J. R., Cosgrove, J. E., Carlson, A. E., and Scire, J. J., 2021, "Acquisition and Processing Considerations for Infrared Images of Rotating Turbine Blades," ASME J. Turbomach., **143**(4), p. 041013.

[37] Moffat, R. J., 1988, "Describing the Uncertainties in Experimental Results," Exp. Therm. Fluid Sci., **1**(1), pp. 3–17.